Dalton Transactions

ROYAL SOCIETY OF CHEMISTRY

PAPER

View Article Online
View Journal | View Issue

Cite this: *Dalton Trans.*, 2025, **54**, 11833

Synthesis, structure, magnetic and transport properties of $CeFeSb_3$†

Manuel Schulze, [a] Bastian Rubrecht, [b] Felix Seewald, [c] Kati Finzel, [a] Bernd Büchner, [b] Anja U. B. Wolter, [b] Hans-Henning Klauss, [c] Thomas Doert *[a] and Michael Ruck [a]

Received 12th June 2025,
Accepted 9th July 2025

DOI: 10.1039/d5dt01387a

rsc.li/dalton

Crystals of $CeFeSb_3$ were synthesised using a Bi-flux. The compound crystallises in the $CePdSb_3$ structure type and contains alternating slabs of Fe-centered Sb octahedra pairs and Sb square layers separated by layers of Ce atoms. Short Fe–Fe distances of 2.682 Å in the octahedra pairs suggest a covalent bond, which was confirmed by quantum chemical calculations. Magnetisation measurements indicate a complex antiferromagnetic ordering at T_N = 4.7 K, attributed to localised Ce 4f moments, likely mediated by RKKY interactions. Mößbauer spectroscopy confirms the non-magnetic behaviour of the Fe atoms. Electrical transport data corroborate $CeFeSb_3$ as a metal with Kondo-like interactions competing with the magnetic ordering.

1. Introduction

Intermetallic antimonides containing rare-earth metal (RE) and transition metal (TM) elements show a large variety of compositions, crystal structures, and interesting physical properties.[1–4] Sb as a heavy p block element on the one hand enables the formation of complex structures with unusual coordination geometries.[5] On the other hand, it shows sizable spin–orbit coupling and, therefore, contributes to the complexity of the physical properties in related compounds.[6] The 3d electrons of the transition metals exhibit a mixed local and itinerant character as their orbitals have a significant spatial extension. This can lead to strong exchange interactions and high magnetic ordering temperatures in corresponding materials. In contrast, the 4f electrons of the heavy RE metals are highly localised, showing weak exchange interactions and low magnetic ordering temperatures. Their strong spin–orbit coupling additionally gives rise to magnetocrystalline anisotropy.[7–11] Therefore, the combined arrangements of TM and RE elements enable complex 3d and 4f electron interactions. In metallic systems, the interaction between the 4f electrons can be mediated by conduction electrons, like itinerant 3d electrons. This includes the exchange-enhancing Rudermann–Kittel–Kasuya–Yosida (RKKY) interaction, leading to higher magnetic ordering temperatures[12–14] and Kondo-like behaviour favouring a non-magnetic ground state.[15,16]

One representative group of such ternary antimonides is formed by the compounds of the composition $RETMSb_3$, which are known for TM = V, Cr, Fe, Co, Ni, and Pd, in combination with the RE elements La–Nd, Sm, Gd, and Tb. Additional members of this group contain Dy or Yb in combination with V and Cr as transition elements. Recent review articles point out the diversity and relevance of this large group of intermetallic compounds.[3,4] The $RETMSb_3$ compounds consist of Sb and RE-square layers, separating $TMSb_6$ octahedra layers with different connecting motives in different structure types. The layered crystal structures result in a pronounced anisotropy of their physical properties, which are easily tuned by small structural deviations and elemental substitutions.

$RECrSb_3$ compounds with RE = Ce–Nd, Sm, and Yb exhibit ferromagnetic ordering temperatures of the Cr 3d magnetic moments above 100 K.[17–25] In contrast, the $RETMSb_3$ containing V, Fe, Ni, or Pd show long-range magnetic ordering of the RE 4f magnetic moments only below 10 K with no contribution of the TM atoms. Except for the ferromagnetic $CeNiSb_3$, the latter compounds order antiferromagnetically.[26–32] Calculations predict similar behaviour for the $RECoSb_3$ compounds.[33] Partial substitution of Sb by Sn seems to suppress the magnetic ordering, resulting in paramagnetic behaviour solely based on the RE 4f electrons in related compounds with TM = Co or Ni.[34,35]

Among the $RETMSb_3$ compounds, those with RE = Ce are of particular interest as the $4f^1$ electron configuration of Ce^{3+} can

[a]*Faculty of Chemistry and Food Chemistry, TUD Dresden University of Technology, 01062 Dresden, Germany. E-mail: thomas.doert@tu-dresden.de*
[b]*Leibniz Institute for Solid State and Materials Research (IFW) Dresden, 01069 Dresden, Germany*
[c]*Institute of Solid State and Materials Physics, TUD Dresden University of Technology, 01062 Dresden, Germany*

†Electronic supplementary information (ESI) available: Crystallographic, spectroscopic, and experimental data. See DOI: https://doi.org/10.1039/d5dt01387a

lead to unique physical properties, including Kondo-like or heavy fermion behaviour.[16] Hence, the $CeTMSb_3$ members usually are well-known in literature and have been extensively characterised for TM = V, Cr, Ni, and Pd.[17,22,27,28,30,31,36] Surprisingly, $CeFeSb_3$ has not been reported alongside the related $REFeSb_3$ compounds.[32] To address this gap, we grew single crystals of $CeFeSb_3$ and report on its synthesis, crystal structure, magnetic and transport properties, and specific heat in the following. Mößbauer spectroscopy and quantum-chemical calculations were employed to further characterise the compound's properties.

2. Experimental

2.1. Synthesis

$CeFeSb_3$ crystals were synthesised *via* a flux-growth method using Bi as flux medium. All starting materials were handled in an argon-filled glove box (MBraun; $p(O_2)/p^0$ < 1 ppm, $p(H_2O)/p^0$ < 1 ppm). Freshly filed Ce (99.9%, Edelmetall Recycling m&k GmbH), Fe powder (99.90%, abcr), Sb flakes (reduced in H_2 stream at 450 °C) and Bi flakes (reduced in H_2 stream at 240 °C) were combined in a 1 : 1 : 3 : 13 (Ce : Fe : Sb : Bi) molar ratio, transferred into a 3 mL silica ampoule, and topped with silica wool as a filter medium for hot centrifugation. The ampoule was sealed using a dynamic vacuum of less than 10^{-2} mbar and placed in a chamber furnace. The reaction mixture was heated to 770 °C and dwelled for 12 h, followed by fast heating to 850 °C, immediate cooling back to 770 °C, and successive cooling at −1 K min^{-1} to 480 °C. The molten flux medium was separated by hot centrifugation, and residual Bi was removed by wet chemical etching in a mixture of acetic acid and hydrogen peroxide (30%) with a volume ratio of 3 : 1.[37] The additional temperature peak to 850 °C is implemented to increase the size of the $CeFeSb_3$ crystals by reducing the initial number of nuclei. Using this method, prismatic $CeFeSb_3$ crystals with up to 1 × 0.5 × 0.3 mm^3 size were obtained. Agglomeration and intergrowth of crystals is, however, a frequent side effect of the flux growth method.

2.2. X-ray diffraction

The crystal structure of $CeFeSb_3$ was examined *via* single-crystal X-ray diffraction (SCXRD). For that, several crystal fragments were mechanically separated from the as-synthesised agglomerates, mounted on glass fibres, and tested for their suitability on a four-circle diffractometer. The final data set used for structure refinements was recorded on an XtaLAB Synergy-S (Rigaku) with microfocus PhotonJet X-ray tube using Ag-Kα radiation (λ = 0.56087 Å) in combination with a hybrid photo counting Eiger3 R1M CdTe detector at 100(2) K. The raw data processing was done with CrysAlisPro, including Lorentz and polarisation factors correction and a multi-scan[38] absorption correction. ShelXT[39] was used to solve the structure, and the structure refinement against F_o^2 was performed with ShelXL[40] under the application of Olex2.[41] Anisotropic displacement parameters were refined for all atoms. Further information on the crystal structure analysis is available from the Fachinformationszentrum Karlsruhe, 76344 Eggenstein-Leopoldshafen (Germany), referencing the depository number CSD-2449824.

The single-crystal diffractometer was further used to determine the crystallographic orientation of three representative crystals exhibiting typical prismatic morphology and size. Based on these measurements, the large faces were identified as perpendicular to the *a*-axis, while the long edges align parallel to the *b*-axis, and the short edges parallel to the *c*-axis.

For powder X-ray diffraction (PXRD), several $CeFeSb_3$ crystals were mechanically extracted and ground to a fine powder <20 μm. The powder was measured under ambient conditions with an Empyrean diffractometer (Malvern PANalytical) in Bragg–Brentano geometry using a curved Ge(111) monochromator and Cu-Kα_1 radiation (λ = 1.540598 Å). Rietveld refinement on the experimental pattern was done with the Jana2020 software[42] to estimate the purity of the sample (Fig. S1, ESI†).

2.3. EDX analysis

Energy-dispersive X-ray (EDX) measurements were performed using a SU8020 (Hitachi) Scanning Electron Microscope (SEM) equipped with an X–Max^N (Oxford Instruments) Silicon Drift Detector (SDD) to analyse the chemical composition of the crystals. The samples were prepared on a carbon pad with distinct crystal faces perpendicular to the electron beam. Elemental mapping was conducted at an accelerating voltage of 20 kV. The EDX results showed a uniform distribution of 20 (1) at% Ce and Fe and 59(1) at% Sb (Fig. S2, ESI†), which closely aligns with the sum formula determined by SCXRD. Minimal traces of the flux medium Bi were detected on the crystal surfaces. Surface oxidation of $CeFeSb_3$ is negligible when exposed to air for weeks.

2.4. Thermal analysis

Differential scanning calorimetry (DSC) was performed in a STA PT 1600 thermal analyser (Linseis) with a platinum measuring head and Al_2O_3 as reference using sealed silica ampoules (0.1 mL). The ground elements incl. Bi as flux material (300 mg in total) in the above stated ratio for the single-crystal syntheses were used to probe the synthesis conditions. The thermal stability of $CeFeSb_3$ was tested on a pelletised powder sample (50 mg). Measurements were performed until T_{max} = 875 °C at a rate of ±2 K min^{-1} (Fig. S3 and S4, ESI†).

2.5. Physical properties measurements

A superconducting quantum interference device (SQUID) from Quantum Design (SQUID VSM and MPMS 3) was used to record magnetisation data of $CeFeSb_3$ crystals between 1.8 K and 400 K. The crystals were attached to a nonmagnetic sample holder and exposed to various external magnetic fields between 10 mT and 7 T. Additionally, the angular-dependent static magnetisation was measured *via* a rotator option. The data were obtained using a zero-field-cooled (zfc) – field-cooled

(fc) sequence in the temperature range from 1.8 to 10 K for various fields up to 7 T.

The specific heat measurements were performed on a mosaic of crystals using a heat-pulse relaxation method with a Physical Property Measurement System (PPMS, Quantum Design). The temperature-dependent signal of the background was measured separately and subtracted.

A direct current resistance (DCR) setup for a cryogen-free measurement system (CFMS; Cryogenic) was employed to measure the temperature-dependent resistivity (T = 2 to 300 K) and magnetoresistance (up to 9 T) of a single $CeFeSb_3$ crystal. Due to the small crystal size, the van der Pauw technique[43] was applied parallel to the *bc*-plane of the crystal using Ag paste in combination with Au wire (50 μm) as contacts.

2.6. Mößbauer spectroscopy

^{57}Fe Mößbauer measurements were conducted using a CryoVac flow cryostat using liquid Helium cooling for the 4.2 K measurement. A Rh/Co source on a WissEL Mößbauer drive unit MR-360 in combination with a DFG-500 frequency generator in sinusoidal mode was used. For detecting and selecting the 14.4 keV gamma rays, a proportional counter tube combined with a WissEL single-channel analyser, Timing SCA was employed. A CMTE multichannel data processor MCD 301/8K was employed for the recording of the Mößbauer spectra. A powder sample of 34 mg $CeFeSb_3$ was investigated at 295 K and 4.2 K. Mößbauer data evaluation has been performed using the analysis program Moessfit[44] utilising a transmission integral fit to account for sample thickness. All center shifts are given relative to α-Fe at room temperature. The linewidth ω is given as half width at half maximum (HWHM).

2.7. Quantum chemical calculations

The electronic band structure was computed at scalar relativistic, closed-shell level with a mesh of 8 × 16 × 8 *k*-points in the Brillouin zone using a modified version of the FPLO22 program.[45] The modification consists of the implementation of the FB16 bifunctional[46] to account for the exchange–correlation effects based on the bifunctional formalism. Subsequent *k*-space analysis was performed with the built-in utilities of the FPLO package.

Scalar relativistic, closed-shell calculations were carried out with a modified version of the FHI-aims package[47] using tight basis sets and a *k*-mesh of 2 × 4 × 2 points in the Brillouin zone and the novel FB16 bifunctional. Subsequent chemical bonding analysis was performed using DGrid[48] with a real space mesh grid of 0.05 Bohr.

3. Results and discussion

3.1. Synthesis

We successfully synthesised single crystals of $CeFeSb_3$ using molten Bi as an inert flux medium. The prismatic crystals, reaching up to 1 mm in length (Fig. 1a), were separated from the flux by hot centrifugation and wet chemical etching.

Bi has been previously employed as a flux for synthesising numerous intermetallic compounds,[49] including other ternary RE–Fe antimonides,[50–52] even though the molten Bi flux pri-

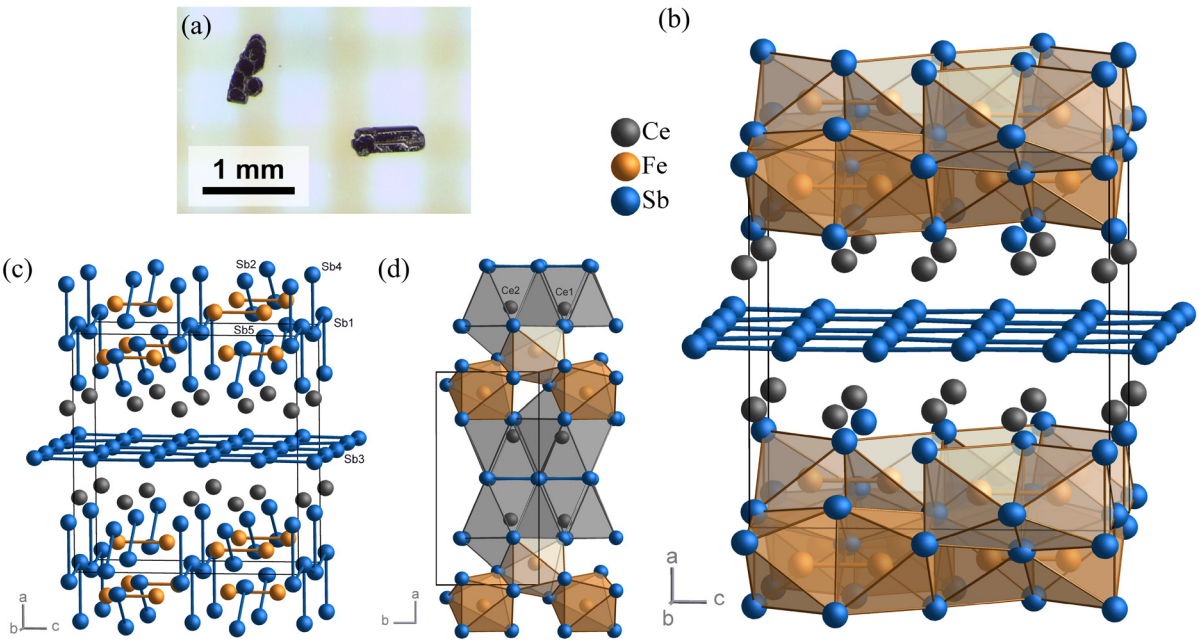

Fig. 1 (a) Flux-grown $CeFeSb_3$ crystals. (b) Crystal structure of $CeFeSb_3$ approximately along the [010] direction with $FeSb_6$ octahedra and Sb(3) plane. (c) Fe–Fe and shortest Sb–Sb distances shown in a ball-and-stick representation; see text for details. (d) Crystal structure along the [001] direction, revealing the two crystallographically inequivalent Ce sites.

marily dissolves Sb[53] and the RE elements,[54] while Fe remains nearly insoluble.[55] Nonetheless, the molten Bi promotes the formation of $CeFeSb_3$ at the applied synthesis conditions below 800 °C, with negligible incorporation into the crystal structure. At temperatures above 800 °C, peritectic decomposition of $CeFeSb_3$ occurs. Formation and decomposition are diffusion-controlled processes without apparent associated temperatures (Fig. S3, ESI†). The decomposition of $CeFeSb_3$ after annealing (Fig. S4, ESI†) and the absence of $CeFeSb_3$ in phase diagrams of the Ce–Fe–Sb system[56] suggest that $CeFeSb_3$ is a metastable phase, stabilised under the non-equilibrium conditions of the Bi-flux growth method used in this work. This characteristic was used to grow larger crystals by shortly increasing the temperature above the empirically determined stability range. Small nuclei are then expected to decompose slightly above the peritectic temperature, while the remaining ones will grow during cooling.

However, binary compounds such as FeSb and $CeSb_2$ are also stable under the synthesis conditions, and their formation could not be entirely suppressed. As already mentioned, agglomeration and intergrowth of crystals occurred frequently and were also observed for crystals of the target phase with binary side phases like $CeSb_2$. This compound in particular was found to obstruct the formation of pure $CeFeSb_3$ crystals due to epitaxial nucleation facilitated by similar structure motifs.[57] A significant excess of Fe in the starting materials does not compensate for the formation of $CeSb_2$ but promotes the formation of FeSb instead.

Despite the reported success of this method, Bi is less commonly used as a flux for the synthesis of $RETMSb_3$ single crystals compared to Sn or Sb self-flux.[4] However, Sn is known to react with some of the starting metals and can therefore be incorporated into the target phases in significant amounts.[34,35] In respective test experiments with Sn as flux medium, the formation of $CeFeSb_3$ was found to be suppressed in favour of Sn-containing phases. Sb self-flux, on the other hand, shifts the elements' ratio, enhancing the formation of $CeFe_4Sb_{12}$ and $CeSb_2$ for the tested synthesis conditions. Overall, neither Sn nor Sb self-flux yielded crystals of $CeFeSb_3$, which may explain why this compound has not been reported in earlier works.

3.2. Crystal structure

The crystal agglomeration and intergrowth mentioned above made the selection of single crystals suitable for crystal structure determination challenging. The crystal used for structure determination consisted of slightly misoriented domains visible as peak splitting with ω-broadening in reconstructed precession images (Fig. S5, ESI†). This is probably the reason for the relatively high residual electron density minima and maxima close to all atomic positions. $CeFeSb_3$ crystallises in the orthorhombic space group *Pbcm* (no. 57) and adopts the $CePdSb_3$ [28] or $LaPdSb_3$ structure type[4,29] (Fig. 1b). This structure is also adopted by other $RETMSb_3$ compounds containing TM = Fe, Co, Ni, and Pd,[28–30,32–35] as summarised in recent contributions.[3,4] The lattice parameters of $CeFeSb_3$ are a = 12.7875(1) Å, b = 6.1774(1) Å, and c = 12.1660(1) Å at 100(2) K (Table 1), aligning with the lanthanide contraction observed in the related $RETMSb_3$ compounds.[32] Atomic coordinates and anisotropic displacements are provided in Table 2, and selected interatomic distances and angles are compiled in Table 3. Note that the atom labelling is chosen according to known $RETMSb_3$ structures for reasons of comparison.[32]

The structure of $CeFeSb_3$ contains one Fe, two Ce, and five crystallographic Sb sites (Table 2). Fe is coordinated by six Sb atoms, forming a distorted octahedron. Two $FeSb_6$ octahedra share a common face perpendicular to [001], resulting in $[Fe_2Sb_9]$ octahedra pairs with a short Fe–Fe distance of 2.682 (1) Å. This distance is close to values found in polynuclear Fe cluster compounds like $Fe_3(CO)_{12}$.[58] Similar short TM–TM distances were also reported for the related $RETMSb_3$ compounds. The $[Fe_2Sb_9]$ octahedra pairs are further linked *via* common edges to form puckered $^2_\infty[FeSb_2]$ slabs in the *bc*-plane at $x \approx 0$. The Sb3 atoms form a slightly distorted $^2_\infty[Sb]$ square net with Sb–Sb distances between 3.008(1) Å and 3.089(1) Å, located parallel to the $FeSb_2$ slabs at $x \approx 0.5$ (Fig. S6a, ESI†). Similar Sb–Sb distances of 3.032(1) Å are

Table 1 Crystallographic data and structural refinement for $CeFeSb_3$

Chemical formula	$CeFeSb_3$
Formula weight	561.22
Space group	*Pbcm* (no. 57)
a [Å]	12.7875(1)
b [Å]	6.1774(1)
c [Å]	12.1660(1)
V [Å^3]	961.035(19)
Z	8
ρ_{calc} [g cm^{-3}]	7.758
Crystal size [mm^3]	0.116; 0.059; 0.042
T [K]	100(2)
Radiation, λ [Å]	Ag-Kα, 0.56087
2θ range [°]	5.03–66.05 (0.51 Å)
Index ranges	$-24 \le h \le 24$
	$-11 \le k \le 11$
	$-23 \le l \le 23$
μ [mm^{-1}]	14.94
Reflections collected	72 930
Independent reflections	3682
R_{int}	0.047
R_1/wR_2 (all data)	0.028/0.071
$\Delta\rho_{max}$ [e Å^{-3}]	3.52
$\Delta\rho_{min}$ [e Å^{-3}]	−5.84
Goof on F_o^2	1.38

Table 2 Atomic coordinates, Wyckoff sites, and anisotropic displacement parameters U_{eq} for $CeFeSb_3$

Atom	Wyckoff position	x	y	z	U_{eq} [Å]
Ce1	4*c*	0.70042(2)	0.25	0	0.00428(4)
Ce2	4*d*	0.30609(2)	0.27541(4)	0.75	0.00422(4)
Fe1	8*e*	0.09971(3)	0.03803(7)	0.86022(4)	0.00455(6)
Sb1	4*c*	0.97237(2)	0.25	0	0.00434(5)
Sb2	4*d*	0.78335(2)	0.26478(4)	0.75	0.00440(4)
Sb3	8*e*	0.50267(2)	0.51245(3)	0.87659(2)	0.00375(4)
Sb4	4*c*	0.21965(2)	0.25	0	0.00422(5)
Sb5	4*d*	0.93932(2)	0.89511(4)	0.75	0.00449(4)

Table 3 Selected interatomic distances and angles for $CeFeSb_3$ at 100 K

Bond	Distance [Å]	Angle	[°]
Ce1–Sb1	3.478(1)	Sb3–Sb3–Sb3	87.04(1)
Ce1–Sb2 (×2)	3.222(1)	Sb3–Sb3–Sb3	90.0
Ce1–Sb3 (×2)	3.340(1)	Sb3–Sb3–Sb3	90.0
Ce1–Sb3 (×2)	3.358(1)	Sb3–Sb3–Sb3	92.90(1)
Ce1–Sb4 (×2)	3.253(1)	Sb5–Fe–Sb1	80.06(1)
Ce2–Sb2	3.232(1)	Sb5–Fe–Sb5	82.67(1)
Ce2–Sb2	3.355(1)	Sb5–Fe–Sb2	88.14(2)
Ce2–Sb3 (×2)	3.292(1)	Sb5–Fe–Sb4	91.30(1)
Ce2–Sb3 (×2)	3.315(1)	Sb1–Fe–Sb2	95.45(2)
Ce2–Sb4 (×2)	3.240(1)	Sb1–Fe–Sb4	97.06(2)
Ce2–Sb5	3.224(1)	Sb2–Fe–Sb4	108.51(2)
Fe–Sb1	2.628(1)	Sb2–Fe–Sb5	112.79(2)
Fe–Sb1	2.694(1)	Sb1–Fe–Sb5	146.24(2)
Fe–Sb2	2.624(1)	Sb5–Fe–Sb4	163.33(2)
Fe–Sb4	2.638(1)		
Fe–Sb5	2.605(1)		
Fe–Sb5	2.629(1)		
Fe–Fe	2.682(1)		
Sb1–Sb1 (×2)	3.169(1)		
Sb1–Sb4	3.162(1)		
Sb2–Sb5	3.032(1)		
Sb3–Sb3	3.008(1)		
Sb3–Sb3	3.080(1)		
Sb3–Sb3	3.089(1)		

found between the Sb2 and Sb5 atoms, which assemble to dumbbells oriented approximately along [120] and [$\bar{1}$20]. Both distances are close to the interatomic distances in elemental Sb (α-As type) of 2.91 Å.[59] The Sb1 and Sb4 atoms form a planar, branched zig-zag chain $^{1}_{\infty}$[Sb] along [010] with a Sb1–Sb1 distance of 3.169 Å and a Sb1–Sb4 distances of 3.162(1) Å. The Sb2–Sb5 dimers are linked to the Sb1/Sb4 chains *via* distances of 3.366(1) Å (Fig. 1c).

The Ce atoms are found between the $^{2}_{\infty}$[$FeSb_2$] double layers and the $^{2}_{\infty}$[Sb] layers. Ce1 is coordinated in a [$CeSb_8$] square antiprism, while Ce2 is located in a [$CeSb_9$] single-capped square antiprism (Fig. 1d). They form slightly distorted $^{2}_{\infty}$[Ce] square layers, assembling extended Ce zig-zag chains along [001] (Fig. S6b, ESI†).

Assigning classical valence states of a metallic compound can only be a coarse approximation. However, based on computational, magnetic, and Mößbauer data (see below), the valence states of the metal atoms can be regarded as +III for Ce and zero for Fe, and −I on average for Sb. The charge distribution within the Sb sublattice can be estimated using the extended Zintl–Klemm concept for nonclassical electron-rich systems.[5] Here, an idealised valence electron count of six (*i.e.*, oxidation state −I) can be assigned to the Sb3 atoms forming the square layers, corresponding to a bonding system of the half-filled $5p_y$ and $5p_z$ orbitals, while the $5p_x$ orbitals form lone-pairs perpendicular to the net. The Sb1–Sb4 chains and the Sb2–Sb5 dimers form an antimony slab with five- and six-connected atoms (Sb1, Sb5) in its central part and one- and two-connected Sb-atoms (Sb2, Sb4) terminating the slab along the *a*-direction towards the Ce atoms.

The number of bonds per atom for the individual Sb sites indicates a gradient of the Sb charges from more negative for the terminating Sb2 and Sb4 atoms adjacent to the Ce layer towards neutral or even slightly positive for the inner Sb1 and Sb5 atoms close to the Fe dimers.

3.3. Quantum chemical calculations

The calculated band structure and density of states (DOS) for $CeFeSb_3$ around the Fermi level are depicted in Fig. 2. A large dispersion for the states close to the Fermi level reflects the strong metallic nature of the system. The high DOS at E_F can be attributed to the Ce 4f states, whereas Fe 4s and 3d and Sb 5p contributions dominate the DOS in the energy range between −2 and 0 eV.

Based on the solid-state calculations obtained from the FHI-aims program, atomic charges were evaluated according to the atoms-in-molecules-theory (AIM).[61] Therefore, the electron density was integrated over the Bader basins after subtracting the nuclear charge *Z*. The calculated Bader charges are generally low. The Bader charge of the Fe atoms is slightly negative (−0.1), which could be translated into an oxidation state between 0 and −I. The Ce1 and Ce2 atoms show positive Bader charges of +1.0 or +1.1. Together with the information from the magnetic data, trivalent Ce can be assumed. The differences in the Bader charges of the Sb atoms are signifi-

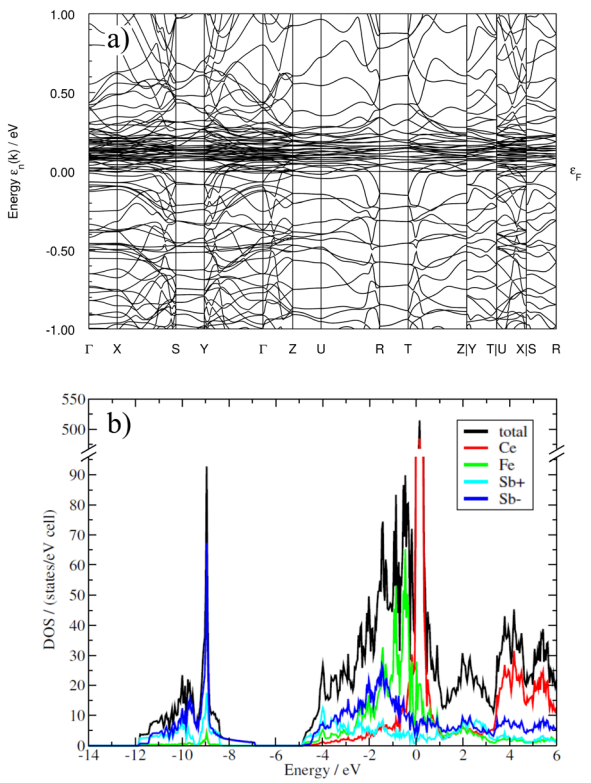

Fig. 2 (a) Calculated band structure and (b) density of states (DOS) of $CeFeSb_3$. The large dispersion of states close to the Fermi level reflects its strong metallic nature; Sb+ and Sb− denote Sb atoms with positive and negative partial charges, respectively.

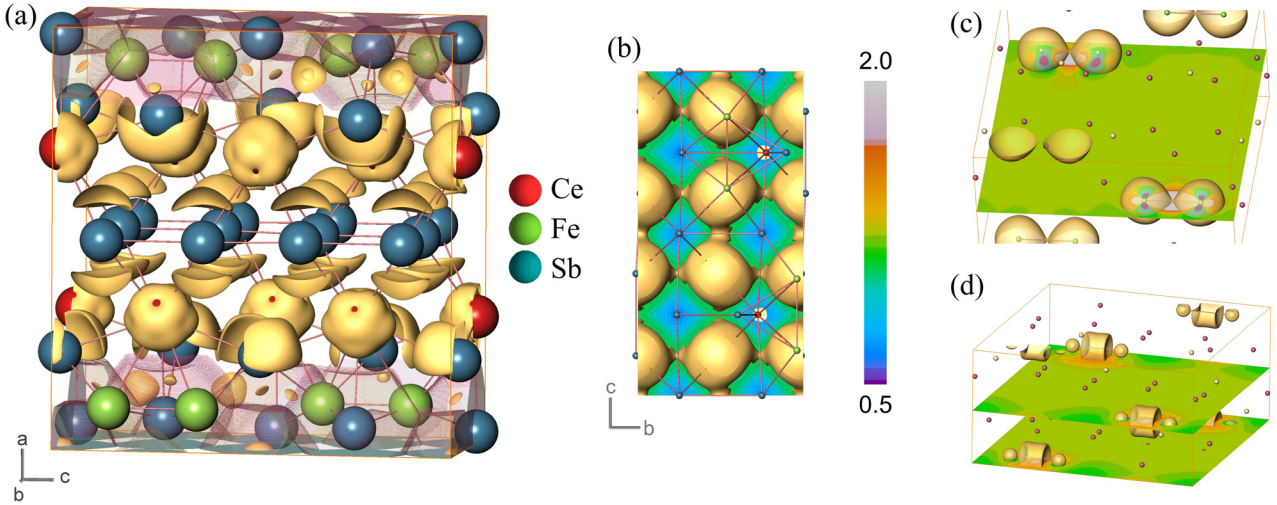

Fig. 3 (a) $CeFeSb_3$ Bader basins for positively charged Sb ions (transparent) and ELI-D at 1.2 a.u. (yellow). (b) ELI-D distribution at 1.08 a.u. representing the chemical bonding situation in the Sb square layer. (c) United electron density for the Fe 3d orbitals and (d) united electron density for the Fe 4s orbitals, each depicted by the isosurface of 0.005 a.u. (yellow). The intersected electron density is shown by the orthoslice in the range of −0.001 to 0.001 in both images.[60]

cant: the Sb2, Sb3, and Sb4 atoms adjacent to the Ce square layers show negative Bader charges of −0.3 and −0.4, hinting towards an oxidation state of −I for each atom. In contrast, the calculated Bader charges for the Sb1 and Sb5 are positive (+0.2 and +0.3), implying an oxidation state between 0 and +I. Thus, the same compound contains negatively and positively charged Sb atoms, acting as electron acceptors and donors. This is in accordance with the considerations based on the extended Zintl–Klemm concept described above.

Fig. 3a shows the Bader basins along with the isosurface of the electron localisability indicator based on the parallel-spin electron pair density (ELI–D)[62,63] at 1.2 a.u. for the Sb atoms. The negatively charged Sb atoms display pronounced irreducible domains, indicating the respective lone pair regions. In contrast, the localisation domains for the lone pair regions of the positively charged Sb atoms are much smaller at this isosurface value. A pronounced localisation domain is observed on the interconnection line between positively (Sb1, Sb5) and negatively (Sb2, Sb4) charged Sb atoms, indicating covalent two-centre bonding between these atoms. The Sb square layers exhibit a prominent multicenter bonding with largely delocalised electrons, as indicated by the flat ELI-D distribution. However, the irreducible domains reveal additional localised two-centre interactions on the interconnection line of the constituent Sb3 atoms. Yet, these covalent interactions are not fully optimised as single irreducible domains in favour of the prominent electron delocalisation within the Sb square layer (Fig. 3b).

Covalent two-centre bonding contributions are also found between the Fe atoms, mainly involving their 3d and 4s electrons (Fig. 3c and d). The clear signature of covalent Fe–Fe bonds supports the interpretation of this structural subunit as Fe_2 dimers. The interactions of the Ce atoms with neighbouring atoms exhibit a mixed bonding character with substantial ionic contributions, reflected by the nearly spherical ELI-D distribution around the Ce atoms. The strongly structured inner-shell features indicate a significant role of the Ce inner electrons to the overall bonding scenario (Fig. S7, ESI†).

3.4. Magnetic properties

Temperature-dependent susceptibility measurements of $CeFeSb_3$ reveal an antiferromagnetic ordering at $T_N \approx 4.7$ K (Fig. 4). A pronounced magnetic anisotropy is observed. Applying a small magnetic field along the crystallographic *b*-axis results in a Néel-like kink, followed by a decrease in magnetisation. In contrast, for fields applied along the *a*- or *c*-axis, the magnetisation shows a more ferromagnetic-like increase below T_N with much higher values for the *a*-axis. In all three directions, the ordering is accompanied by a zero-field cooled-field-cooled splitting.

The high-temperature susceptibility data in the range of 100 K to 400 K were analysed using the modified Curie–Weiss law, $\chi(T) = \chi_0 + C/(T - \theta_{CW})$, yielding an effective magnetic moment of $\mu_{eff} = 2.2(2)\mu_B$ for all three crystallographic axes. This value is slightly below the calculated effective magnetic moment $\mu_{cal} = 2.54\mu_B$ for free Ce^{3+} ions, indicating that the magnetisation is primarily governed by strongly localised Ce^{3+} electron moments. Remarkably, the Fe electrons show no significant contribution to the gross magnetic moments. This suggests a non-magnetic spin configuration for the Fe atoms, likely stabilised by the covalent bonding in the Fe_2 dimers. The extracted temperature-independent susceptibility χ_0 is approximately 0.01 emu mol^{-1} Oe^{-1}, while typical metals exhibit values in the range of $\sim 10^{-3}$ to 10^{-4} emu mol^{-1} Oe^{-1} due to Pauli paramagnetism of free elec-

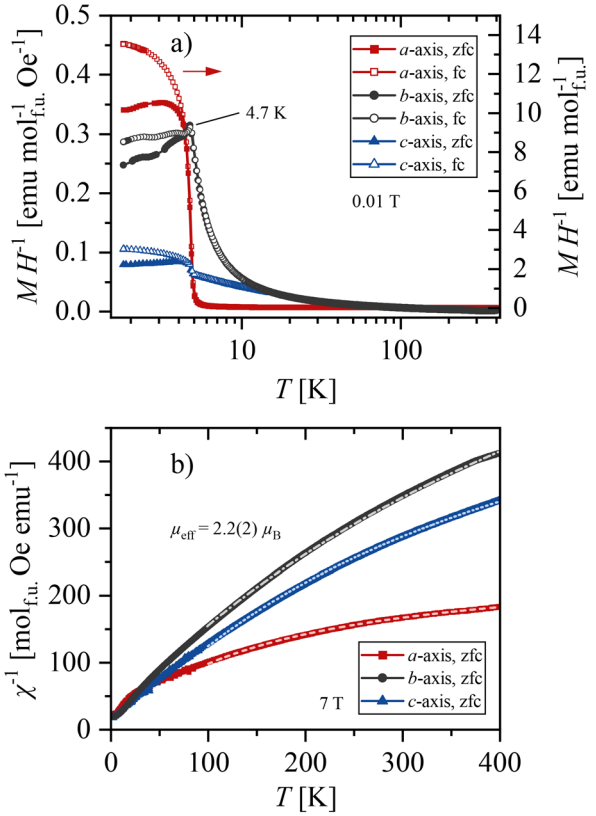

Fig. 4 (a) Temperature-dependent susceptibility and (b) inverse susceptibility of $CeFeSb_3$, broken lines represent the modified Curie–Weiss fits.

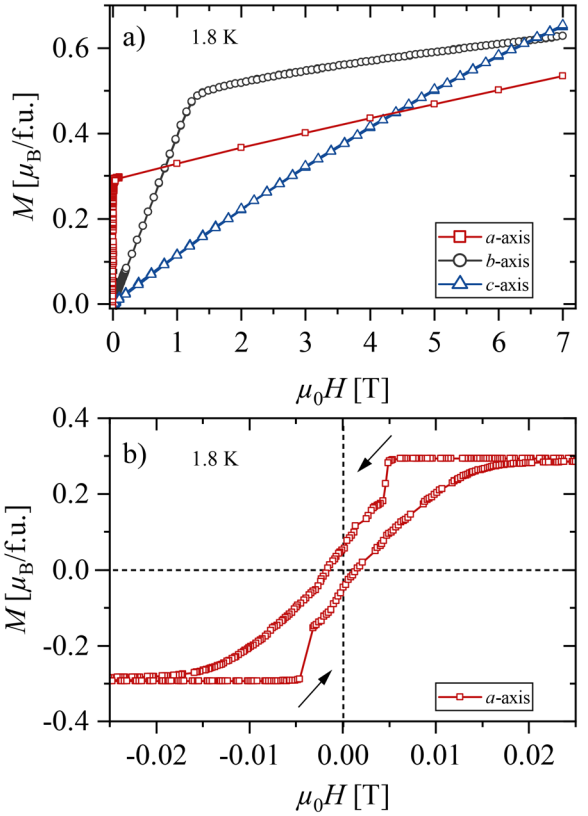

Fig. 5 (a) Field-dependent magnetisation of $CeFeSb_3$ at T = 1.8 K for the three crystallographic directions, (b) field-dependent magnetisation at T = 1.8 K with the magnetic field applied parallel to the a-axis revealing hysteretic behaviour at small fields.

trons. This deviation suggests an additional contribution to the susceptibility, possibly by partially broken Fe_2 dimers at higher temperatures, leading to a slow onset of thermal excitations already observable in the high-temperature susceptibility data. While the Curie–Weiss fit yields reasonable values for μ_{eff} and χ_0, consistent with other experimental data, the yielded Curie–Weiss temperatures are non-conclusive. The obtained values around zero were highly sensitive to the fitting range, possibly due to thermal excitations of Fe-dimer states at higher temperatures mentioned above. Therefore, we refrain from further discussing the fitted values for θ_{CW} here.

Fig. 5a shows the field-dependent magnetisation along the three principal crystallographic directions at 1.8 K. In an applied field along the b-axis, the moment increases linearly up to ~$0.5\mu_B$ f.u.$^{-1}$ at 1.1 T in line with the antiferromagnetic spin alignment along this direction. Above this field, the slope decreases sharply, and the moment increases to ~$0.6\mu_B$ f.u.$^{-1}$ at 7 T. Along the c-axis, the moment steadily increases to ~$0.65\mu_B$ f.u.$^{-1}$ at 7 T, with a slight curvature over the entire field range. In contrast, with field applied along the a-axis, the moment increases steeply at low fields, reaching ~$0.3\mu_B$ f.u.$^{-1}$ at 20 mT already. A zoom-in of the low-field region reveals a small hysteresis loop with a slight bow-tie shape (Fig. 5b). Specifically, during the down sweep, the moment abruptly drops at around 5 mT, and correspondingly abruptly increases at approximately −5 mT during the up sweep. For fields above 20 mT, the moment increases linearly, reaching ~$0.5\mu_B$ f.u.$^{-1}$ at 7 T. A linear dependence of $M(H)$ in rare-earth magnets is typically attributed to a van Vleck contribution, which is expected to be isotropic. In contrast, $CeFeSb_3$ shows anisotropic values of approximately $0.035(1)\mu_B$ f.u.$^{-1}$ T^{-1} along the a-axis and $0.020(1)\mu_B$ f.u.$^{-1}$ T^{-1} along the b-axis. Moreover, the anisotropic behaviour observed in all three principal crystallographic directions indicates a non-trivial anisotropy landscape.

To further analyse this anisotropic magnetic behaviour observed in $\chi(T)$ and $M(H)$, angle-resolved magnetisation measurements were performed at 3 K in a field of 1 T (Fig. 6). The magnetisation changes continuously as the field is tilted out of the Ce square net. While the slope is flatter close to the a-axis, it reverses sharply when the field angle passes through the b- or c-axis. Within the bc-plane, the magnetisation adjusts smoothly with a slight slope change around 45°, where the field aligns with the shortest Ce–Ce interatomic distances. Although the exact magnetic structure of $CeFeSb_3$ remains unresolved, the direction-dependent $\chi(T)$ and $M(H)$ data suggest a non-collinear antiferromagnetic spin structure within the Ce square nets in the crystallographic bc-plane.

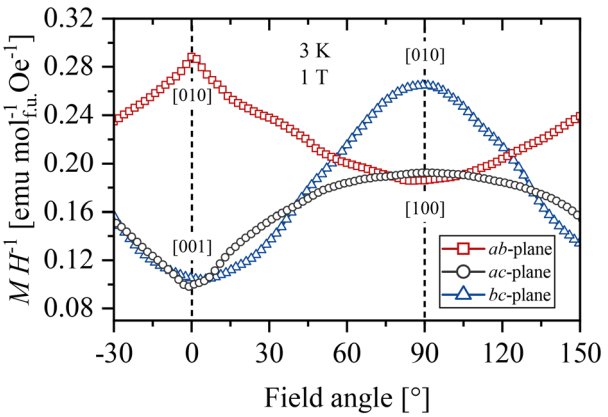

Fig. 6 Angular dependence of the magnetisation for the *ab*-, *ac*-, and *bc*-plane at T = 3 K in a field of $\mu_0 H$ = 1 T.

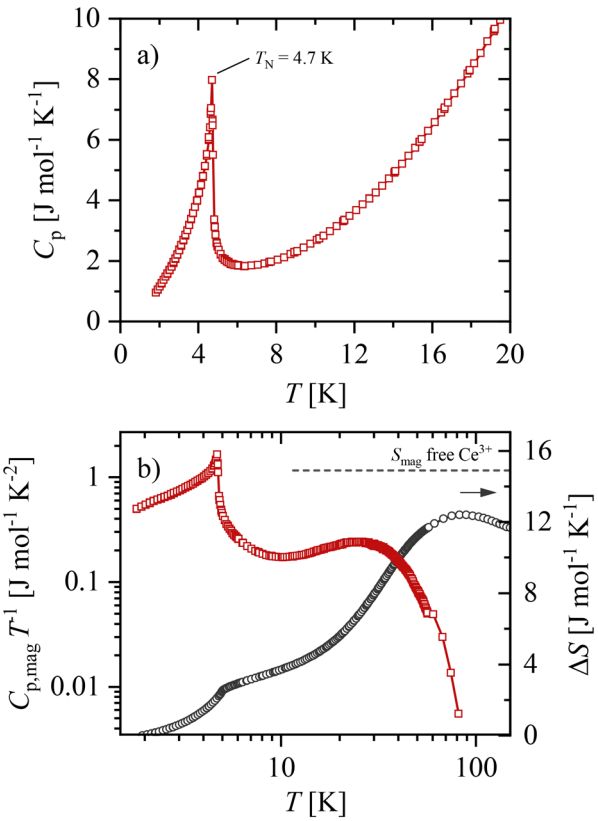

Fig. 7 (a) Temperature-dependence of the specific heat and (b) temperature-dependence of the magnetic contribution of the specific heat divided by temperature and released magnetic entropy of $CeFeSb_3$ at zero magnetic field.

While an antiferromagnetic interchain spin alignment along the *b*-direction could result in the Néel-like kink in $\chi(T)$, a ferromagnetic-like spin alignment may be present along the extended zig-zag chains in the *c*-direction when applying an external field. The steep moment increase along the *a*-axis in $M(H)$ at small fields indicates an easy spin alignment out of the Ce layers and, therefore, a significant ferromagnetic spin component along this direction. The small hysteresis loop further implies a ferromagnetic spin component aligned between the Ce nets and pinned along this direction by an uniaxial anisotropy.

The strong anisotropy and complex behaviour can be explained by the RKKY exchange interaction, which is based on the indirect magnetic coupling of localised magnetic moments by conduction electrons. The strength and periodicity of the RKKY interaction depend on the Fermi surface and conduction electron density along different *k*-space directions. Similar effects were reported for the related $REFeSb_3$ compounds.[32] Additionally, the magnetic interaction of the Ce moments in this structure type appears to be crucially influenced by the transition metal elements. While antiferromangetic ordering with pronounced anisotropy was also confirmed for $CePdSb_3$,[28] $CeNiSb_3$ exhibits ferromagnetic ordering.[30]

3.5. Heat capacity

Fig. 7a shows the temperature-dependence of the specific heat below 20 K at zero applied magnetic field. In agreement with the magnetisation measurements, a sharp lambda peak marks the onset of the long-range magnetic order below 4.7 K.

To extract the magnetic contribution to the specific heat, the data above 100 K was fitted using a combination of a Debye and a linear part to model the phononic and the electronic contribution to the specific heat, respectively (Fig. S8, ESI†). The extracted magnetic contribution $C_{p,mag}$ T^{-1} is shown in Fig. 7b. The suppression of static magnetic order above 4.7 K is associated with an entropy release of at least 3 J mol^{-1} K^{-1}. However, as our measurement range is limited to 1.8 K, a sizeable amount of entropy is not accounted for. Considering this limitation, the low-temperature entropy release approaches the expected value of 5.76 J mol^{-1} K^{-1} for an effective spin $s_{eff} = \frac{1}{2}$ system (Fig. 7b). This is consistent with Ce^{3+} being a Kramers ion, where the $s_{eff} = \frac{1}{2}$ ground state doublet dominates the magnetic behaviour at low temperatures.

In addition to the magnetic ordering peak, $C_{p,mag}$ T^{-1} shows a broad maximum around 30 K. This feature is commonly observed in rare-earth compounds and arises from the thermal population of higher crystal-electric field levels. Integrating over the whole temperature range accounts for 85% of the entropy expected for a free Ce^{3+} ion, *i.e.*, $R{\cdot}\ln(2J + 1)$ with J = 5/2. This observation is in line with the reduced effective moment in the Curie–Weiss fits of the temperature-dependent magnetisation, corresponding to a partial delocalisation of the Ce 4f electrons and an absence of any Fe contributions to μ_{eff}.

3.6. Mößbauer spectroscopy

Mößbauer spectra recorded at 295 K and 4.2 K are shown in Fig. 8. In both cases, the signal can be described by a

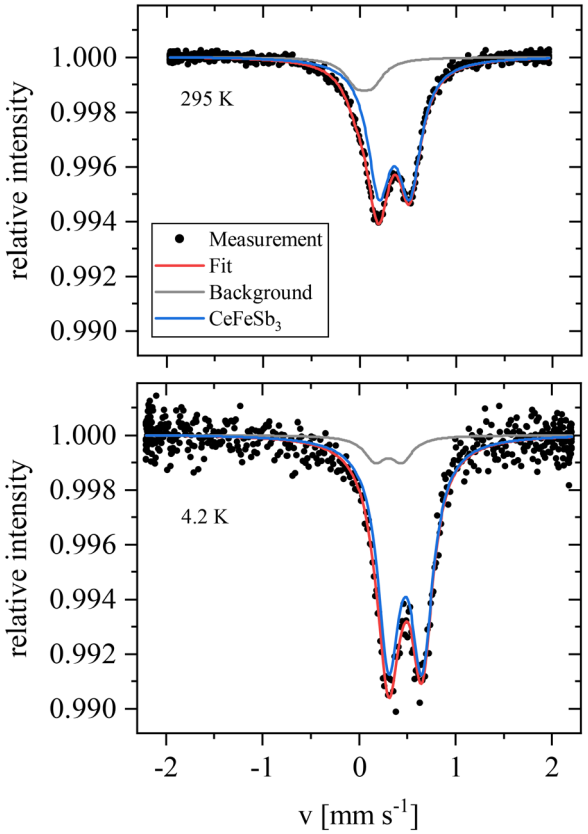

Fig. 8 ^{57}Fe-Mößbauer spectra of $CeFeSb_3$ at 295 K and 4.2 K, indicating non-magnetic behaviour of the Fe atoms. The background signal primarily originates from steel components of the cryostat employed in the measurements. Additionally, a minor contribution from FeSb may be present as evidenced by Rietveld refinement (Fig. S1, ESI†).

single quadrupole split Mößbauer site. Assuming an electric field gradient (EFG) with the principle components $\|V_{zz}\| \geq \|V_{yy}\| \geq \|V_{xx}\|$ and an asymmetry parameter of $\eta = (V_{xx} - V_{yy})V_{zz}^{-1} = 0$, we obtain V_{zz} = 19.14(16) V Å^{-2} at 295 K and V_{zz} = 20.90(30) V Å^{-2} at 4.2 K. The half-width at half-maximum (HWHM) linewidth is ω = 0.143(4) mm s^{-1} at 295 K and ω = 0.137(6) mm s^{-1} at 4.2 K. There is no indication of a static magnetic hyperfine field at the Fe position or magnetic-induced line broadening by transferred fields. Therefore, the Mößbauer data are in line with the magnetisation data by confirming the non-magnetic behaviour of Fe.

The center shifts of CS = 0.468(4) mm s^{-1} at 295 K and CS = 0.588(7) mm s^{-1} at 4.2 K are in the typical range for Fe-containing intermetallic compounds.[64,65] These values can be rationalised with an Fe^0 state with s = 0 configuration,[66] in agreement with the calculated Bader charges and the magnetic properties. However, the positive isomer shifts indicate reduced s-electron density near the Fe nuclei,[67] which can be attributed to the Fe 4s electron localisation in the covalent Fe–Fe bonds as well as the shift of electron density to the Fe 3d states.

3.7. Transport properties

The temperature-dependent electrical resistivity of $CeFeSb_3$ was measured within the *bc*-plane of the crystals, and is shown in Fig. 9a. Above 75 K, the resistivity decreases slightly with decreasing temperature. Below 75 K, the slope of the resistivity curve gets steeper, reaching a minimum around 15 K, followed by an increase with a local maximum at $T_N \approx 4.7$ K. The logarithmic increase in resistivity below 15 K, although only over a narrow temperature range (inset in Fig. 9a), is a typical Kondo-like behaviour implying the screening of the localised Ce 4f moments by conduction electrons below 15 K.[68] In the antiferromagnetic state, below $T_N \approx 4.7$ K, the RKKY interaction becomes dominant over the spin–flip scattering of the conduction electrons, effectively decreasing the resistivity. The temperature-dependent resistivity of $CeFeSb_3$ is in line with the transport properties observed in related $RETMSb_3$ compounds.[26,28,30,32,34]

The field-dependent magnetoresistance (MR) of $CeFeSb_3$ is shown in Fig. 9b. The electric current and magnetic field were applied parallel to the *bc*-plane and the *a*-axis, respectively. Below the antiferromagnetic ordering temperature of $T_N \approx$ 4.7 K, $CeFeSb_3$ shows negative MR, indicating reduced spin-disorder scattering of the conduction electrons due to the alignment of the magnetic moments within the external field.

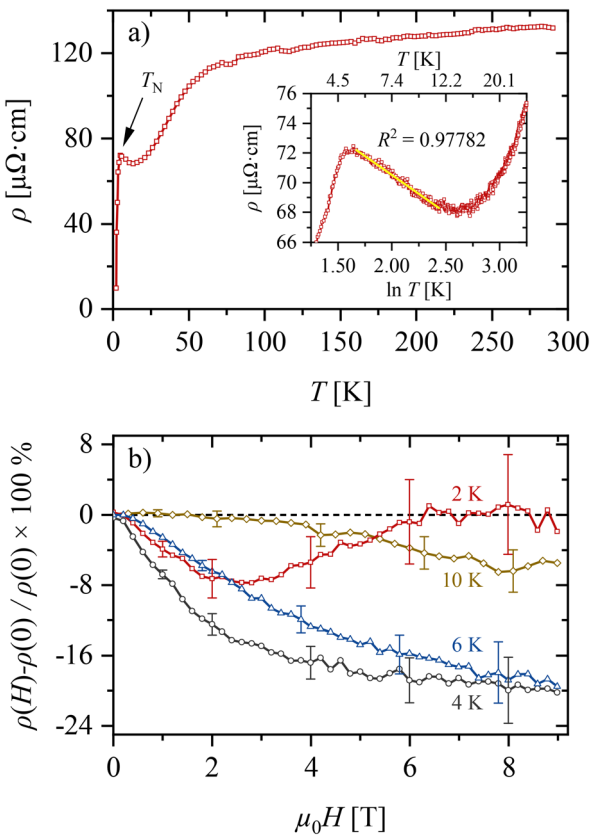

Fig. 9 (a) Temperature-dependent resistivity and (b) magnetoresistance of $CeFeSb_3$ with the electric current and magnetic field applied parallel to the *bc*-plane and the *a*-axis, respectively.

The magnitude of the negative MR is largest near T_N, where thermal fluctuations are still present, and the external field effectively affects disordered spins. At lower temperatures, the antiferromagnetic structure becomes increasingly stable and spin-disorder scattering is intrinsically suppressed, reducing the influence of the external field. Therefore, at 2 K the magnitude of negative MR is small, as the magnetic structure is fully stable, and a gradual increase of MR towards a plateau around 0% is observed for an external field larger than 2 T. In this range, the spin alignment of the external field is negligible or may even slightly perturb the antiferromagnetic structure. Additionally, Lorentz-force-induced deflection of conduction electrons may contribute to increased resistivity in higher fields.[69]

In the paramagnetic state above T_N, the magnitude of the negative MR decreases when the temperature is increased. This suggests suppressed Kondo-scattering of the conduction electrons by the localised Ce 4f moments in an external magnetic field.[70]

4. Conclusion

The new compound $CeFeSb_3$ was synthesised using the Bi-flux method. $CeFeSb_3$ crystallises in the $CePdSb_3$ structure type and consists of $^2_\infty[FeSb_2]$ double layers of $[Fe_2Sb_9]$ octahedra pairs and $^2_\infty[Sb]$ square layers separated by square layers of Ce atoms. Quantum chemical calculations indicate charge transfer from the Ce atoms to the Sb atoms and covalent bonds between the nearly uncharged Fe atoms, which can be understood as covalently bonded Fe_2 dimers. This is in good agreement with the Mößbauer spectra, which further prove the non-magnetic behaviour of the Fe atoms. The antiferromagnetic ordering at $T_N \approx 4.7$ K can, thus, be solely attributed to the Ce 4f magnetic moments, probably mediated by the conduction electrons *via* RKKY interaction. Electrical transport measurements show metallic conductivity and indicate Kondo-like interactions competing with the magnetic ordering. Direction-dependent magnetisation measurements show a strong, non-trivial magnetocrystalline anisotropy of the material. The data suggest a non-collinear antiferromagnetic spin alignment between the extended zig-zag chains within the Ce square nets in the *bc*-plane. Ferromagnetic spin alignment might be between the nearest neighbours in the zig-zag chains and along the *a*-axis. The exact magnetic structure of $CeFeSb_3$ and the related $RETMSb_3$ compounds is subject to future investigations.

The characterisation of $CeFeSb_3$ closes a gap within the series of $RETMSb_3$ compounds. Its structural and physical properties are consistent with those in the related compounds, as well as the complex behaviour based on the Ce^{3+} spin-$\frac{1}{2}$ configuration. Nonetheless, the different magnetic ordering compared to $CeTMSb_3$ with TM = Ni or Pd emphasises the tunability of these compounds' magnetism by substituting the TM element within the same crystallographic structure type. The synthesis and characterisation of $CeTMSb_3$ compounds with partially substituted TM elements would, thus, be interesting to track the transition between the different magnetic structures.

Conflicts of interest

The authors declare no conflict of interest.

Data availability

The data supporting this article have been included in the ESI.† Crystallographic data for $CeFeSb_3$ is available from the Fachinformationszentrum Karlsruhe, 76344 Eggenstein-Leopoldshafen (Germany), under the depository number CSD-2449824.

Acknowledgements

The authors acknowledge financial support by the Deutsche Forschungsgemeinschaft through the Collaborative Research Center SFB 1143 "Correlated Magnetism: From Frustration to Topology" (project-id. 247310070) and the Würzburg–Dresden Cluster of Excellence on "Complexity and Topology in Quantum Matter – ct.qmat" (EXC 2147, project-id. 390858490).

References

1 O. L. Sologub and P. S. Salamakha, *Handb. Phys. Chem. Rare Earths*, Elsevier Science B.V., Amsterdam, 2003, vol. 33.
2 E. L. Thomas, J. N. Millican, E. K. Okudzeto and J. Y. Chan, *Comments Inorg. Chem.*, 2006, **27**, 1–39.
3 A. Kumar Singh, S. Sarkar and S. C. Peter, *Chem. Rec.*, 2022, **22**, e202100317.
4 B. K. Rai, P. O'Rourke and U. N. Roy, *J. Phys.: Condens. Matter*, 2022, **34**, 273002.
5 G. A. Papoian and R. Hoffmann, *Angew. Chem., Int. Ed.*, 2000, **39**, 2408–2448.
6 A. N. Rudenko, M. I. Katsnelson and R. Roldán, *Phys. Rev. B*, 2017, **95**, 081407(R).
7 J. P. Liu, F. R. de Boer, P. F. de Châtel, R. Coehoorn and K. Buschow, *J. Magn. Magn. Mater.*, 1994, **132**, 159–179.
8 M. D. Kuz'min and A. K. Zvezdin, *J. Appl. Phys.*, 1998, **83**, 3239–3249.
9 R. Skomski and D. J. Sellmyer, *J. Rare Earths*, 2009, **27**, 675–679.
10 A. V. Andreev, Y. Skourski, M. D. Kuz'min, S. Yasin, S. Zherlitsyn, R. Daou, J. Wosnitza, A. Iwasa, A. Kondo, A. Matsuo and K. Kindo, *Phys. Rev. B: Condens. Matter Mater. Phys.*, 2011, **83**, 184422.
11 S. Mugiraneza and A. M. Hallas, *Commun. Phys.*, 2022, **5**, 95.
12 M. A. Ruderman and C. Kittel, *Phys. Rev.*, 1954, **96**, 99–102.
13 T. Kasuya, *Prog. Theor. Phys.*, 1956, **16**, 45–57.

14 K. Yosida, *Phys. Rev.*, 1957, **106**, 893–898.
15 J. Kondo, *Prog. Theor. Phys.*, 1964, **32**, 37–49.
16 K. Yamada, K. Yosida and K. Hanzawa, *Prog. Theor. Phys.*, 1984, **71**, 450–457.
17 K. Hartjes, W. Jeitschko and M. Brylak, *J. Magn. Magn. Mater.*, 1997, **173**, 109–116.
18 L. Deakin, M. J. Ferguson, A. Mar, J. E. Greedan and A. S. Wills, *Chem. Mater.*, 2001, **13**, 1407–1412.
19 D. D. Jackson, M. Torelli and Z. Fisk, *Phys. Rev. B: Condens. Matter Mater. Phys.*, 2001, **65**, 014421.
20 S. J. Crerar, L. Deakin and A. Mar, *Chem. Mater.*, 2005, **17**, 2780–2784.
21 D. D. Jackson and Z. Fisk, *Phys. Rev. B: Condens. Matter Mater. Phys.*, 2006, **73**, 024421.
22 D. D. Jackson, S. K. McCall, A. B. Karki and D. P. Young, *Phys. Rev. B: Condens. Matter Mater. Phys.*, 2007, **76**, 064408.
23 M. Inamdar, A. Thamizhavel and S. Ramakrishnan, *Phys. Rev. B: Condens. Matter Mater. Phys.*, 2008, **77**, 132410.
24 M. Inamdar, A. Thamizhavel and S. Ramakrishnan, *J. Phys.: Condens. Matter*, 2008, **20**, 295226.
25 K. H. Chow, W. A. MacFarlane, Z. Salman, I. Fan, S. J. Crerar, A. Mar, M. Egilmez, J. Jung, B. Hitti and D. Arseneau, *Phys. B*, 2009, **404**, 615–618.
26 R. T. Macaluso, D. M. Wells, R. E. Sykora, T. E. Albrecht-Schmitt, A. Mar, S. Nakatsuji, H. Lee, Z. Fisk and J. Y. Chan, *J. Solid State Chem.*, 2004, **177**, 293–298.
27 E. L. Thomas, R. T. Macaluso, H.-O. Lee, Z. Fisk and J. Y. Chan, *J. Solid State Chem.*, 2004, **177**, 4228–4236.
28 A. Thamizhavel, H. Nakashima, T. Shiromoto, Y. Obiraki, T. D. Matsuda, Y. Haga, S. Ramakrishnan, T. Takeuchi, R. Settai and Y. Ōnuki, *J. Phys. Soc. Jpn.*, 2005, **74**, 2617–2621.
29 E. L. Thomas, D. P. Gautreaux and J. Y. Chan, *Acta Crystallogr., Sect. E: Struct. Rep. Online*, 2006, **62**, i96–i98.
30 E. L. Thomas, D. P. Gautreaux, H.-O. Lee, Z. Fisk and J. Y. Chan, *Inorg. Chem.*, 2007, **46**, 3010–3016.
31 A. S. Sefat, S. L. Bud'ko and P. C. Canfield, *J. Magn. Magn. Mater.*, 2008, **320**, 120–141.
32 W. A. Phelan, G. V. Nguyen, A. B. Karki, D. P. Young and J. Y. Chan, *Dalton Trans.*, 2010, **39**, 6403–6409.
33 W.-Z. Cai, L.-M. Wu, L.-H. Li and L. Chen, *Eur. J. Inorg. Chem.*, 2009, 230–237.
34 D. P. Gautreaux, C. Capan, J. F. DiTusa, D. P. Young and J. Y. Chan, *J. Solid State Chem.*, 2008, **181**, 1977–1982.
35 W. A. Phelan, G. V. Nguyen, J. F. DiTusa and J. Y. Chan, *J. Alloys Compd.*, 2012, **523**, 176–181.
36 M. Leonard, S. Saha and N. Ali, *J. Appl. Phys.*, 1999, **85**, 4759–4761.
37 *CRC handbook of metal etchants*, ed. P. Walker, CRC Press, Boca Raton, 1991.
38 R. H. Blessing, *Acta Crystallogr., Sect. A: Found. Crystallogr.*, 1995, **51**(Pt 1), 33–38.
39 G. M. Sheldrick, *Acta Crystallogr., Sect. A: Found. Crystallogr.*, 2015, **71**, 3–8.
40 G. M. Sheldrick, *Acta Crystallogr., Sect. C: Cryst. Struct. Commun.*, 2015, **71**, 3–8.
41 O. V. Dolomanov, L. J. Bourhis, R. J. Gildea, J. A. K. Howard and H. Puschmann, *J. Appl. Crystallogr.*, 2009, **42**, 339–341.
42 V. Petříček, L. Palatinus, J. Plášil and M. Dušek, *Z. Kristallogr.*, 2023, **238**, 271–282.
43 L. J. van der Pauw, *Phillips Res. Rep.*, 1958, **13**, 1–9.
44 S. Kamusella and H.-H. Klauss, *Hyperfine Interact.*, 2016, **237**, 82.
45 K. Koepernik and H. Eschrig, *Phys. Rev. B: Condens. Matter Mater. Phys.*, 1999, **59**, 1743–1757.
46 K. Finzel and A. I. Baranov, *Int. J. Quantum Chem.*, 2017, **117**, 40–47.
47 V. Blum, R. Gehrke, F. Hanke, P. Havu, V. Havu, X. Ren, K. Reuter and M. Scheffler, *Comput. Phys. Commun.*, 2009, **180**, 2175–2196.
48 M. Kohout, *DGrid, Version 5.0*, 2016.
49 R. Pöttgen, *Z. Kristallogr. - Cryst. Mater.*, 2025, **240**, 127–139.
50 W. A. Phelan, G. V. Nguyen, J. K. Wang, G. T. McCandless, E. Morosan, J. F. DiTusa and J. Y. Chan, *Inorg. Chem.*, 2012, **51**, 11412–11421.
51 F. Pabst, S. Palazzese, F. Seewald, S. Yamamoto, D. Gorbunov, S. Chattopadhyay, T. Herrmannsdörfer, C. Ritter, K. Finzel, T. Doert, H.-H. Klauss, J. Wosnitza and M. Ruck, *Adv. Mater.*, 2023, **35**, e2207945.
52 F. Pabst, Dissertation, TUD Dresden University of Technology, Germany, 2023.
53 D. Minić, D. Manasijević, D. Živković, J. Stajić-Trošić, J. Đokić and D. Petković, *Mater. Sci. Technol.*, 2011, **27**, 884–889.
54 K. Yoshihara, J. B. Taylor, L. D. Calvert and J. G. Despault, *J. Less-Common Met.*, 1975, **41**, 329–337.
55 D. Boa, S. Hassam, G. Kra, K. P. Kotchi and J. Rogez, *CALPHAD: Comput. Coupling Phase Diagrams Thermochem.*, 2008, **32**, 227–239.
56 D. Zhu, C. Xu, C. Li, C. Guo, R. Zheng, Z. Du and J. Li, *J. Alloys Compd.*, 2018, **731**, 1125–1139.
57 R. Wang and H. Steinfink, *Inorg. Chem.*, 1967, **6**, 1685–1692.
58 F. A. Cotton and J. M. Troup, *J. Am. Chem. Soc.*, 1974, **96**, 4155–4159.
59 C. S. Barrett, P. Cucka and K. Haefner, *Acta Crystallogr*, 1963, **16**, 451–453.
60 K. Finzel and U. Schwarz, *Inorg. Chem.*, 2024, **63**, 20217–20225.
61 R. F. W. Bader, *Atoms in Molecules: A Quantum Theory*, Oxford University Press, Oxford, 1990, vol. 22.
62 M. Kohout, K. Pernal, F. R. Wagner and Y. Grin, *Theor. Chem. Acc.*, 2004, **112**, 453–459.
63 F. R. Wagner, V. Bezugly, M. Kohout and Y. Grin, *Chem. – Eur. J.*, 2007, **13**, 5724–5741.
64 V. V. Nemoshkalenko, O. N. Rasumov and V. V. Gorskii, *Phys. Status Solidi B*, 1968, **29**, 45–48.
65 A. M. van der Kraan and K. Buschow, *Phys. B+C*, 1986, **138**, 55–62.
66 N. E. Erickson and A. W. Fairhall, *Inorg. Chem.*, 1965, **4**, 1320–1322.

67 E. Fluck, W. Kerler and W. Neuwirth, *Angew. Chem.*, 1963, **75**, 461–472.
68 A. C. Hewson, *The Kondo Problem to Heavy Fermions*, Cambridge University Press, 1993.
69 J. Smit, *Physica*, 1951, **17**, 612–627.
70 U. Rauchschwalbe, F. Steglich, A. de Visser and J. Franse, *J. Magn. Magn. Mater.*, 1987, **63–64**, 347–350.